Intermetallics 178 (2025) 108621

Contents lists available at ScienceDirect

Intermetallics

journal homepage: www.elsevier.com/locate/intermet

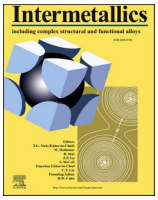

NbMoVTa refractory high-entropy alloy incorporated WNi matrix composite as a future plasma-facing material: Evaluation of mechanical properties and helium ion irradiation behavior

Burçak Boztemur [a], Kaan Filiz [a], Zahide Karagüney [a], Eyüpcan Gökaydın [a], Yasin Bozkurt [a], Ceren Özbasmacı [a], Kübra Gürcan Bayrak [b], Yue Xu [c], Laima Luo [c], Duygu Ağaoğulları [a,*], M. Lütfi Öveçoğlu [a,d,**]

[a] Istanbul Technical University, Faculty of Chemical and Metallurgical Engineering, Department of Metallurgical and Materials Engineering, Particulate Materials Laboratories (PML), Graphene & 2D Materials Laboratory, Maslak, Istanbul, 34469, Türkiye
[b] Eskişehir Technical University, Faculty of Engineering, Department of Materials Science and Engineering, Iki Eylül Campus, 26555, Eskişehir, Türkiye
[c] School of Materials Science and Engineering, Hefei University of Technology, Hefei, 230009, China
[d] MEF University, Department of Mechanical Engineering, Maslak, Istanbul, 34396, Türkiye

ARTICLE INFO

Keywords:
Refractory high-entropy alloys
Mechanical alloying
Plasma-facing material
Mechanical properties
He^+ irradiation resistance

ABSTRACT

Refractory high-entropy alloys (RHEAs) have gained attention in the last decades with their high mechanical strength, self-healing mechanism, and high irradiation resistance. These materials are evaluated to have a high potential as plasma-facing materials for fusion reactors. In this study, helium ion irradiation and mechanical behaviors of the RHEA-reinforced WNi matrix composites were investigated based on this perspective. Equimolar molybdenum, niobium, tantalum and vanadium powders were mechanically alloyed for 6 h to produce NbMoVTa RHEA with a single BCC phase. Then, different amounts (10, 20, 30, and 40 wt%) of RHEA were added into the W1Ni (containing 99 wt% W and 1 wt% Ni) matrix by planetary ball milling for 72 h. Consolidation was conducted by spark plasma sintering technique (1410 °C, 1 min). X-ray diffraction, scanning electron microscopy coupled with energy dispersion spectroscopy, and Archimedes' density analyses were performed on the composites. Moreover, wear and hardness properties of the composites were examined, and the lowest specific wear rate (0.59 $mm^3/N.m \times 10^{-5}$) and the highest hardness value (10.10 GPa) were found for the W1Ni-40RHEA composite. Helium irradiation was exposed to the composites to observe their irradiation resistance. It was observed that the lowest increment and the least deformation were obtained with the SPS'ed W1Ni-40RHEA composite. With the analysis of He^+ irradiation, it was determined that the effect of radiation on mechanical properties is irrelevant. Also, it was observed that the addition of RHEA into the W matrix can create a high potential for using plasma-facing material. Moreover, it decreased the problems of tungsten against He^+ irradiation.

1. Introduction

Population growths and changes in living standards have led to an increase in the need for energy all over the world in addition that, new environmentally friendly, non-climatic and unlimited resources are needed such as solar, wind, hydroelectric, geothermal or nuclear energy [1–4]. Among these, the nuclear energy that is classified as fission and fusion are types of renewable energy obtained from the nucleus of the atom. The fission reaction, which is limited due to the production of harmful wastes, produces energy as a result of the splitting atoms of radioactive elements such as uranium [4,5]. On the other hand, energy production with the fusion reaction allows less harmful waste to be produced, the prevention of accidents that may occur as a result of the spontaneous stopping of the reaction, and enables more energy

* Corresponding author.
** Corresponding author. Istanbul Technical University, Faculty of Chemical and Metallurgical Engineering, Department of Metallurgical and Materials Engineering, Particulate Materials Laboratories (PML), Graphene & 2D Materials Laboratory, Maslak, Istanbul, 34469, Türkiye
E-mail addresses: bozkurtdu@itu.edu.tr (D. Ağaoğulları), ovecoglu@itu.edu.tr (M.L. Öveçoğlu).

https://doi.org/10.1016/j.intermet.2024.108621
Received 27 September 2024; Received in revised form 6 December 2024; Accepted 21 December 2024
Available online 31 December 2024

production [6]. Fusion reactors that provide energy production by performing the fusion reaction that includes deuterium and tritium transforation into plasma and the released energy is used [3,7]. Of different fusion reactor parts, the divertor is the most exposed to high-energy plasma. Thus, divertors are defined as plasma-facing materials [8,9]. Plasma-facing materials must be suitable for harsh operation conditions, handle a large heat flux, be compatible with intense magnetic fields, minimize plasma contamination, and be cost-effective [10,11].

Tungsten (W) as a refractory metal having high melting point, high sputtering threshold, good corrosion resistance, and high tensile strength, high sputtering erosion resistance, suppressed tritium retention, and reduced neutron activation is ideally suited for fusion applications [12–15]. So, tungsten is the best candidate material for the first wall plasma-facing application [16]. However, despite these excellent properties, W has low fracture toughness, radiation-induced embrittlement, and high ductile to brittle transition temperature (DBTT) during plasma exposure [17,18]. Furthermore, the DBTT increases significantly under neutron irradiation because of embrittlement caused by lattice damage and transmutation [19,20]. In addition, W has loss of strength and suffers from volatile oxidation above ~1000 °C, which totally limits its fusion application as the temperature on the divertor surface is expected to reach nearly 1100 °C under transient conditions [18,21,22]. Moreover, these problems create blistering at moderate temperatures by deuterium and helium and the formation of pits, holes, and bubbles by helium at process temperature on the tungsten surface [23,24]. These limitations demand further research to improve tungsten and their alloys for using in fusion applications. Some alloying elements (Re, Ta, V, Ti, Mo, Cr, etc.) have been added into the W matrix in order to overcome these problems, and there are many studies about this topic (W-Re [25], W-V [26], W-Cr [27] and W-Ta [28], etc.). Kwak et al. [27] reported that the W-Cr composites exhibited superior high-temperature strength and ductility compared to pure metals, as individually a high DBTT and intergranular fracture indicate that pure W is brittle, but plastically deformed patches, slip lines, and river patterns indicate that pure Cr displayed pseudo-ductile behavior due to local plastic yield. Also, Cui et al. [28] observed that the W irradiation behavior was enhanced with the addition of Ta. Although adding elements to tungsten somewhat eliminated the deficiencies, it could not completely solve the problems.

Refractory high-entropy alloys (RHEAs) have several characteristics that are better than those of conventional alloys and a resultant single-phase due to their high mixing entropy [29–34]. The goal of combining multiple principal elements in RHEAs is to create a solid solution with high entropy and better technical properties. These include excellent resistance to corrosion, oxidation, and creep, as well as excellent mechanical strength, hardness, and thermal stability [35–37]. This implies the fact that they could work well in applications where they come into contact with plasma and high temperature [38,39]. Heat dissipation, defect formation, and defect mobility processes are impacted by the unexpected microstructural simplicity and compositional complexity of RHEAs [40–42]. The RHEA structure undergoes spontaneous amorphization and recrystallization, which reduce the defects in its structure, named as self-healing effect. Since the self-healing mechanism is very important against the irradiation deformation [41–43], the utilization of refractory high-entropy alloys as reinforcement in the W matrix can improve the properties of pure tungsten for use as a plasma-facing material. Moreover, W-rich refractory high-entropy alloys have higher irradiation resistance thanks to their self-healing mechanism. Cui et al. [43] reported that the irradiation resistance of pure tungsten was increased by adding of TaVCrTi RHEA. Furthermore, Waseem et al. [44] showed that the $W_xTaTiVCr$ RHEA exhibited better irradiation properties than pure tungsten.

Despite its excellent preoperties, the high melting point poses a challenge for the production of tungsten. In the literature, vacuum arc melting [45–47], spark plasma sintering [48–50], pressureless sintering [51–53], and selective laser melting [54] are preferred methods in the production of W-based materials. Among these methods, spark plasma sintering (SPS) is generally used for consolidation thanks to provide high mechanical properties and fast production. So far, different RHEAs (WNbMoTaV [55], NbMoTaWVCr [56], TiZrNbMoTa [57], NbMoTaWVTi [58], TaNbHfZrTi [59], TiVNbZrHf [60]) have been produced using SPS. However, the sintering temperature of tungsten is very high because of its high melting point, so the activated sintering has been used at lower sintering temperatures to improve sinterability. In activated sintering, metal with a low melting temperature (a variety of transition metals such as Co, Ni, Pt, Fe, and Pd) must be dissolved in a metal with a high melting temperature [61–65]. By doing this, the sintering path is shortened, and the process is facilitated, which leads to a high densification rate in the final product [66]. In particular, due to its ductile behavior, Ni is very effective in decreasing the brittleness of tungsten against plasma. Currently, there exist various studies carried out specifically on the activated sintering of W-based composites which were reinforced with oxides (La_2O_3, Y_2O_3, HfO_2, Sm_2O_3, ThO_2), borides (TiB_2, HfB_2, CrB_2, MoB_2), and carbides (TiN, ZrC, TiC, HfC) [67–70]. All these composites exhibited better microstructural and mechanical properties than those of pure W [67–69,71–74]. Qin et al. [66] reported the activated sintering of TiNbMoTaW RHEA with Ni by using SPS. Also, Shivakumar et al. [75] proved that the Ni-activated sintering was very effective in the densification of a MoNbTaW RHEA. Although activated sintering is the most beneficial method for increasing the sinterability of RHEA, there are few studies in the literature. Therefore, investigating the effect of activated sintering on RHEAs and facilitating their production is of unique value.

Although tungsten is the best option for the plasma-facing materials in the divertor component, it has some problems such as low fracture toughness, radiation-induced embrittlement, and high DBTT against to He^+ irradiation. To overcome these problems, the RHEAs that have self-healing mechanisms, high melting points, high corrosion resistance, and high strength can be reinforced into the W matrix. So, the thermodynamic calculations were conducted on the refractory elements based on the oxidation behavior. It can be understood that all refractory elements have a higher oxygen affinity than tungsten, and it is very important for the volatile problem of W. Moreover, Ni-activated sintering to lower the sintering temperature of tungsten and reduce its brittleness makes tungsten matrix composite production highly efficient. So, better mechanical properties, lower sintering temperature, higher densification, and higher helium irradiation resistance can be obtained. The different amounts of equimolar NbMoVTa RHEA were produced, and reinforced into pre-alloyed W1Ni (99 wt% W and 1 wt% Ni) via mechanical alloying (MA). After characterization studies such as XRD, SEM/EDS, particle size and pycnometer density analysis, the composite powders were activated sintered by spark plasma sintering method. The composites were analyzed in terms of microstructural (XRD, SEM/EDS), mechanical (Archimedes' density, Vickers microhardness and wear properties), and He^+ irradiation resistance properties. Furthermore, it is understood that the RHEA reinforced WNi composite can be a promising plasma-facing material in order to be used in divertor part.

2. Experimental procedure

2.1. Raw materials and sample processing

W (supplied from AEM, 99.9 % purity, <45 μm, ICSD Card No: 96-900-6487, Bravais lattice: body-centered cubic, a = 0.317 nm), Ni (supplied from Alfa Aesar, 99.9 % purity, 3–7 μm, ICSD Card No: 96-210-0647, Bravais lattice: face-centered cubic, a = 0.352 nm), Mo (supplied from Alfa Aesar, 99.9 % purity, particle size <45 μm, ICSD Card No: 96-900-8544, Bravais lattice: body-centered cubic, a = 0.315 nm), Nb (supplied from Alfa Aesar, 99.9 % purity, particle size <45 μm, ICSD Card No: 96-411-1970, Bravais lattice: body-centered cubic, a = 0.333 nm), Ta (supplied from Alfa Aesar, 99.9 % purity, particle size <45 μm, ICSD Card No: 96-900-8553, Bravais lattice: body-centered

cubic, a = 0.331 nm) and V (supplied from Alfa Aesar, 99.9 % purity, particle size <45 μm, ICSD Card No: 98-008-9673, Bravais lattice: body-centered cubic, a = 0.303 nm) powders were used as raw materials. XRD patterns of W, Ni, Mo, Nb, Ta, and V elemental powders with 2Θ values and their characteristic peaks are given as supplementary information (Fig. S1). The equimolar NbMoVTa RHEA powder blends were weighed in the Kern™ PLJ Precision Balance. The RHEA powders and WC balls (ø 6.5 mm) were placed into WC vials (50 ml) with a ball-to-powder weight ratio (BPR) of 10:1. In order to prevent oxidation, the vials with powders mixture and balls were sealed in a glovebox (Plas Labs™) filled with Ar gas. The WC vials and balls were coated with the same composition by mechanical alloying (MA, SPEX™ 8000D Mixer/Mill) for 4 h at 800 rpm in order to avoid WC impurities which might come from vials and balls. The RHEA powder blend was mechanically alloyed for 6, 8, and 10 h. 2 wt% stearic acid ($C_{18}H_{36}O_2$) was added into the RHEA powders mixture during milling to prevent agglomeration and sticking of powders to the vial. The annealing process was carried out on the 6 h mechanically alloyed (MA'ed) RHEA powders in a low-temperature tube furnace (MTI DTF™ 1200X Tube Furnace) at 750 °C and 900 °C for holding times of 7 and 9 h under Ar atmosphere to remove stearic acid and to provide homogenization. Both of the heating and cooling rates were 10 °C/min during annealing. The matrix alloy powders blended as 99 wt% W and 1 wt% Ni were placed with WC balls (ϕ 6.5 mm) and the 10:1 BPR into WC vials (500 ml). After sealing in the glovebox that has an Ar atmosphere, the pre-alloyed W1Ni powders were obtained at 400 rpm for 72 h MA in the planetary (Fritsch/Pulverisette™ 5 Classic Line Planetary Ball Mill). These MA processes are shown in Fig. 1. End of these processes, W1Ni matrix was reinforced with the different amounts (10, 20, 30, and 40 wt %) of RHEA powders by using 72 h milling. The powders subjected to MA were designated as MA'ed W1Ni, W1Ni-10RHEA, W1Ni-20RHEA, W1Ni-30RHEA, and W1Ni-40RHEA powders hereafter. The activated sintering of MA'ed powders were performed by spark plasma sintering (SPS, FCT HPD™ 25/I, FCT Systeme GmbH) performed at 1410 °C for 1 min (Fig. 1). The MA'ed powders were placed into a cylindrical graphite mold (ø 20 mm). The cooling/heating rates during SPS were 100 °C/min until 600 °C. Samples were held for 5 min at 600 °C. After that, the temperature reached 1410 °C for 1 min at 90 °C/min and the samples were cooled in a vacuum atmosphere. The starting pressure was at 14 MPa and increased to 30 MPa. The SPS'ed samples are hereafter referred to as SPS'ed W1Ni, W1Ni-10RHEA, W1Ni-20RHEA, W1Ni-30RHEA and W1Ni-40RHEA. After SPS, the precision cutting of samples was done by wire erosion (SPM™ SP640-P Wire Erosion) based on the determined dimensions (10 × 5 × 1 and 10 × 10 × 1 mm) for the He^+ irradiation test. The remaining parts of the same samples were used for the mechanical tests.

2.2. Characterization

X-ray diffraction method (Bruker™ D8 Advanced Series XRD) was used for the phase analyses of MA'ed powders and SPS'ed samples with CuK_α radiation (λ = 0.154 nm, 35 kV, and 40 mA), 2Θ range of 10–90°, step size of 0.02°, and rate of 2°/min. The crystalline phases were identified by using powder diffraction files of the International Center for Structure Database® (ICSD). The average crystallite sizes and lattice strains of the MA'ed powders were determined with the software (Bruker AXS DIFFRAC.TOPAS™ 4.2) and the modified Scherrer's formula [76]. Based on the XRD patterns, Rietveld analyses were performed to define the approximate phase fractions of the samples. The particle size distributions of the powders were measured in a particle size analyzer (Microtrac™ Stabino Nano-flex). Multiple measurements were performed to ensure high accuracy. The ultrasonic stirring (Bandelin™ Sonopuls) was used to prevent the formation of particle agglomeration. The densities of the MA'ed powders were measured by a gas pycnometer (Micromeritics AccuPyc™ II 1340) in a 1 cm^3 sample chamber at room temperature using He gas (Linde™, 99.996 % purity) as the displacement medium. The densities of SPS'ed samples were measured in the alcohol media based on Archimedes' principle (Shimadzu™ precision balance equipped with the apparatus). The scanning electron microscope (SEM, Thermoscientific™ Quattro S), mounted with electron dispersive spectroscopy (EDS), was used to analyze the microstructures of materials. Also, grain size measurement was realized with Image-J software.

2.3. Mechanical tests

The density of the sintered samples was determined by Archimedes' method in an ethanol media. The microhardness testing (Schimadzu™ Vickers HMV) of the SPS'ed samples was performed for 10 s under 500 g (4.903 N). In order to the hardness values of the samples to be high accurate, an average of 25 indentations were taken. Also, the hardness values were determined by taking the average of these values and standard deviations. Indentations of the SPS'ed samples were imaged by an optical microscope (OM, Nikon™ Eclipse). Reciprocating wear tests of SPS'ed samples were carried out in a tribotester (Tribotechnic™ ball-on-disc) at room temperature under a 4 N load using a 6 mm diameter hardfacer of Al_2O_3 ball. Wear testing conditions were selected as: 6 mm/s sliding speed, 20 m sliding distance, and 2 mm wear track length. Wear volume loss values were measured with the wear track 2-D profiles screened by a surface profilometer (Veeco™ Dektak 6 M).

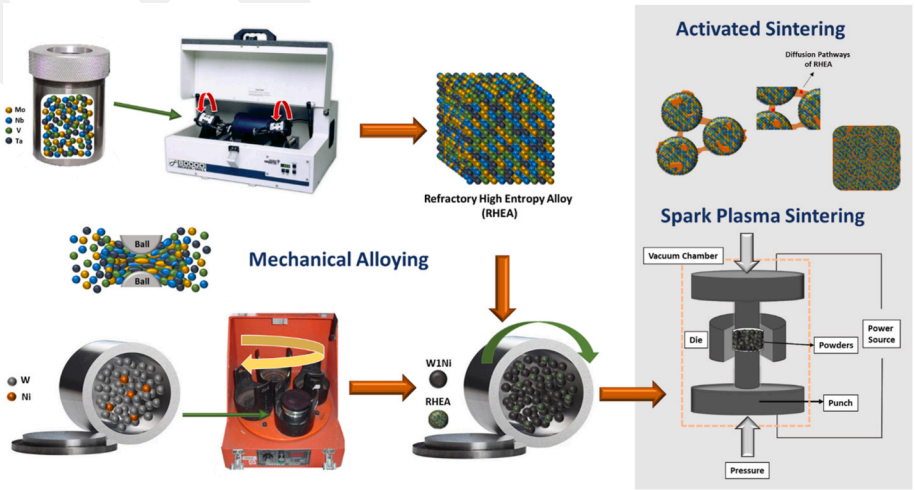

Fig. 1. Schematic representation for the production process of RHEA-reinforced WNi matrix composites.

2.4. Helium ion irradiation test

The SPS'ed samples were exposed to He^+ irradiation tests in a plasma-surface interaction system under extreme conditions (PSIEC) [77]. The SPS'ed samples were subjected to 50 -eV He^+ irradiation with a flux of 1.102×10^{21} ions/(m^2s). The 1.983×10^{24} ions/m^2 irradiance fluence was set for 30 min for each sample. During the exposure process, the surface temperature of all SPS'ed samples reached to ~423 K. SEM/EDS and XRD analyses were done on irradiated samples to examine microstructural changes and phase formations after irradiation. Also, irradiation deformation was determined with cross-section images. Moreover, hardness measurements were conducted on the irradiated sample to observe increments because of defects and deformations.

3. Results and discussion

3.1. Thermodynamic calculations

The Ellingham diagram is helpful to understand the equilibrium in heterogeneous systems including metal, its oxide, and gas phase. In the plasma conditions, oxidation behavior is very important for the volatility of tungsten oxide. Moreover, oxidation affinity plays an important role among RHEAs. Every metal has the different heat capacity (C_p) that is shown in Eq. (1), and this difference is very effective on the Gibbs free energy calculation. The Gibbs free energy of each refractory metal and its oxide involved was calculated as a function of the temperature of enthalpy and entropy using Eq. (2) - Eq. (3). ΔG_T° is known from the previous calculation, since it is a state function and its value does not change with the reaction path. The standard reference state was set for each element of the alloy, i.e. the stable phase of the element at each computed temperature (T for 25 °C < T < 1900 °C). For the oxidation of refractory metals, the Ellingham diagram was directly obtained the Gibbs free energy (ΔG_T°) from Eq. (4) versus temperature, by subtracting ΔG_T° of reagents to ΔG_T° of the products for the oxidation reaction. These values were calculated as "product-reactant" calculations according to Aydın et al.'s study [78].

$$C_P = a + b.T + c.\ T^{-2} \tag{1}$$

$$\Delta S_T^\circ = \Delta S_{298}^\circ + \int_{298}^{T} \frac{C_P}{T}.\ dT \tag{2}$$

$$\Delta H_T^\circ = \Delta H_{298}^\circ + \int_{298}^{T} C_P.\ dT \tag{3}$$

$$\Delta G_T^\circ = \Delta H_T^\circ - T.\Delta S_T^\circ \tag{4}$$

In addition, the Ellingham diagram oxidation and carburization of the mostly used refractory metals with Al, and W, Mo, V, Nb, and Ta elements that are used in this study were drawn based on these calculations (Fig. 2a–d). These reactions are exothermic at room temperature, and the entropy values of them are negative. Furthermore, the slopes of these lines give the negative entropy changes in the equation, and all slopes in the graph are positive. So that, the entropy changes are negative for the oxidation and carburization reactions, and the entropy is decreasing after oxidation and carburization. It can be understood that these reactions can not actualize at room temperature, and it is becoming hard with increasing temperature. However, the bottom reaction is more likely to be realized if oxygen is present in these multiple systems, because it has the lowest Gibbs free energy. Moreover, the higher Gibbs free energy means that the equation is reversible and the more impossible for that material to happen. Based on these thermodynamic calculations, Fu et al. [79] reported the TiO formation for ball milled and spark plasma sintered TaNbVTi refractory high-entropy alloy system. Fig. 2a shows that Ti element has the higher possibility for oxidation as compared to Ta, Nb, and V elements. Also, Ouyang et al. [80] studied on the $Ti_{38}V_{15}Nb_{23}Hf_{24}$ system at different oxidation temperatures, and observed that HfO_2 phase at 1000 °C oxidation temperature. Also, Boztemur et al. [52] worked on the W-Nb- Mo-V-Ta system, and

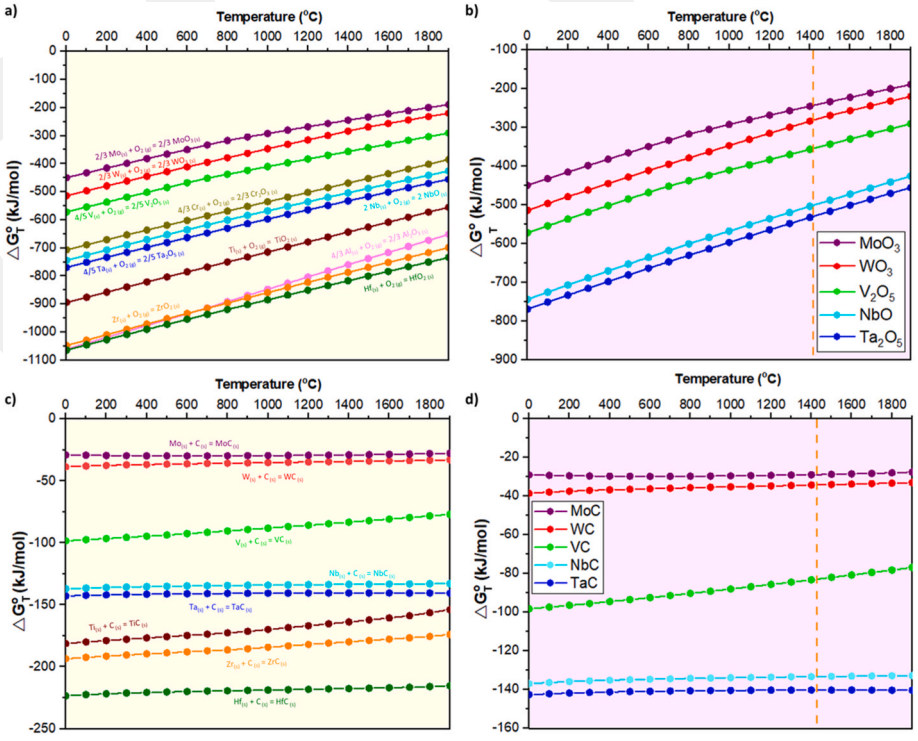

Fig. 2. The Ellingham diagram of (a, b) metal/oxide and (c, d) metal/carbide for the mostly used refractory metals with Al and the W, Mo, V, Nb, and Ta elements that are used in this study. The dashed line represents 1410 °C that is process temperature.

observed Ta_2VO_6 and Al_2O_3 phases for WNbMoVTaCr and WNbMoVTaAl systems, respectively. In this study, Ta elements must be first oxidized for the Nb-Mo-V-Ta system (Fig. 2b), and then V and Nb elements will start to be oxidized. Furthermore, there is no difference from the beginning for oxidation by adding into the W matrix at sintering temperature (1410 °C) because the W element has the highest Gibbs free energy for oxidation. According to the calculation, Nb and Ta were highly possible to be oxidized and carburized between W, Mo, Nb, Ta and V elements because of the lowest Gibbs free energy values. So, some volatility problems for tungsten in the plasma-wall interaction can be solved with the addition of refractory high-entropy alloys.

3.2. Characterization of the MA'ed W1Ni-MoNbVTa powders

Elemental Nb, Mo, V, and Ta powders were mechanically alloyed (MA'ed) for 6, 8 and 10 h at 800 rpm in order to synthesize the single BCC phase in the microstructure. XRD patterns of the as-blended and mechanically alloyed powders are shown in Fig. 3a. According to the results, all the elemental peaks were detected in the XRD of as-blended. Phase formation that is named BCC1 started with 6 h. However, WC (ICSD Card No: 96-210-0646, Bravais lattice: hexagonal close-packed, a, b = 0.289 nm and c = 0.283) contamination due to WC balls and vials was also observed with increasing milling times in addition to the BCC1 phase. This contamination amount was measured by Rietveld analysis (Fig. 3b). While minimum contamination was obtained with 6 h milling as 15.7 wt%, this value increased to 41.8 wt% WC impurity after 10 h milling. Cui et al. [43] used mechanical alloying (BPR: 10:1, 400 rpm, and 25 h) in order to create $W_x(TaVCrTi)_y$ RHEAs. Also, Waseem et al. [44] reported that the production of $W_xTaTiVCr$ RHEA was provided with the MA in plastic vials (BPR: 1:1, 30 rpm, and 3 h). WC contamination was not observed in these investigations because of low milling speed and different milling media. However, Liu et al. [81] observed the WC contamination after milling a MoNbTaW RHEA for 30 h with WC balls in a WC vial (BPR: 20:1 and 400 rpm). Similarly, Gu et al. [82] showed that the WC contamination was obtained after 30 h ball milling. Moreover, Boztemur et al. [52] pointed out the WC contamination occurred after milling for 6 h (BPR: 10:1 and 800 rpm) of the WNbMoVTa RHEA powders. In this study, a shorter time of 6 h of milling time was chosen as optimum in order to get rid of WC contamination and BCC1 phase formation. Moreover, the annealing method was preferred for the phase homogenization and the evaporation of stearic acid that is added during milling. Xiang et al. [83] tried different annealing temperatures (400, 500, 600, 700, and 800 °C) for a TiZrNbTa HEA to achieve the best yield strength results. Also, some studies [84] showed that good mechanical behavior was obtained at 600–700 °C. The optimization attempts were made for annealing at different temperature (750 and 900 °C) and duration (7 and 9 h). Based on the XRD results (Fig. 3c), the annealing parameters were examined. The $(Ta,Nb)O_x$ phase (ICSD Card No: 98-001-0745, Bravais lattice: tetragonal primitive, a, b = 0.476 nm and c = 0.916 nm) was observed after the annealing process because of system oxygen. When the annealing process was applied for 7 h at 900 °C, a high amount of $(Ta,Nb)O_x$ phase was observed compared to the other parameters. Increasing of the temperature and time affected the $(Ta,Nb)O_x$ phase amount. However, the intensity of BCC1 peaks rose with increasing annealing time. The Rietveld analysis was conducted on these powders (Fig. 3d). Then, it is observed that the amount of oxide phase increased with increasing temperature and duration for the annealing. So that, 9 h annealing at 750 °C was chosen for optimum annealing time, and was applied for the RHEA powders before sintering.

Tungsten is one of the best candidate material for plasma-facing applications [85–87]. However, its high melting point poses a big challenge for the production methods. To overcome this problem and to conduct sintering of W at low temperatures, activated sintering techniques have been used by adding small amounts of nickel and/or titanium (~1–2 wt%) to W and the sintering has been achieved in the vicinity of 1500 °C [88,89]. In a previous study, where 1 wt% Ni was added to 99 wt% W powders to provide activated sintering, Boztemur et al. [70] observed that 72 h planetary ball mill conditions (BPR: 10:1 and 400 rpm) provided better results compared to shorter periods of 24 and 48 h. Based on this, pre-alloyed W1Ni powders mechanically alloyed for 72 h were used as the matrix alloy, which was reinforced with various amounts of RHEA powders (10, 20, 30, and 40 wt%) MA'ed for 6 h and annealed at 750 °C for 9 h. XRD analysis of the MA'ed W1Ni and W1Ni-XRHEA powders (X = 10, 20, 30, and 40) are shown in Fig. 4a, revealing a single BCC2 phase for all samples. Fig. 4b shows enlarged (110) peaks of the BCC2 phase, which shifted to higher Bragg angles with increasing amounts of reinforcement and, thus, to lower lattice constant values [91]. This is in good agreement with Wang et al. [90] who expressed that increasing the V concentration in $V_xNbMoTa$ causes the XRD pattern to shift slightly to higher 2θ values, indicating the decreased lattice constant as estimated by Bragg's Law ($2d\sin\theta = n\lambda$). While tungsten has 0.141 nm atomic radius, Nb, Mo, Ta, and V have 0.147, 0.140, 0.147, and 0.135 nm atomic radius, respectively [91]. Except for V, the equimolar RHEA elements in our investigation have roughly the same atomic radius as tungsten, and when reinforcement increases, the peak shifts to the right (higher Bragg angle values), resulting in lattice shrinkage. Furthermore, Cui et al. [43] reported the peaks shifting to the right with increasing amounts of TaVCrTi in the W matrix. The RHEA powders had lower density values than the tungsten, so the density of composite powders decreased with increasing amount of reinforcement RHEA (Fig. 4c). While the W1Ni powder's density was

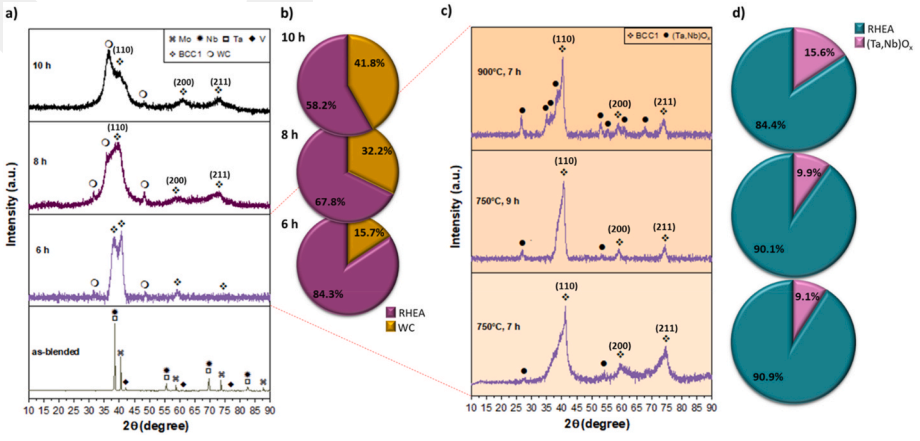

Fig. 3. (a) XRD patterns of the as-blended, 6, 8, and 10 h MA'ed Nb, Mo, Ta, V powders, (b) their corresponding Rietveld analysis, (c) XRD patterns, and (d) their corresponding Rietveld analysis of the annealed RHEA powders at different temperature and duration.

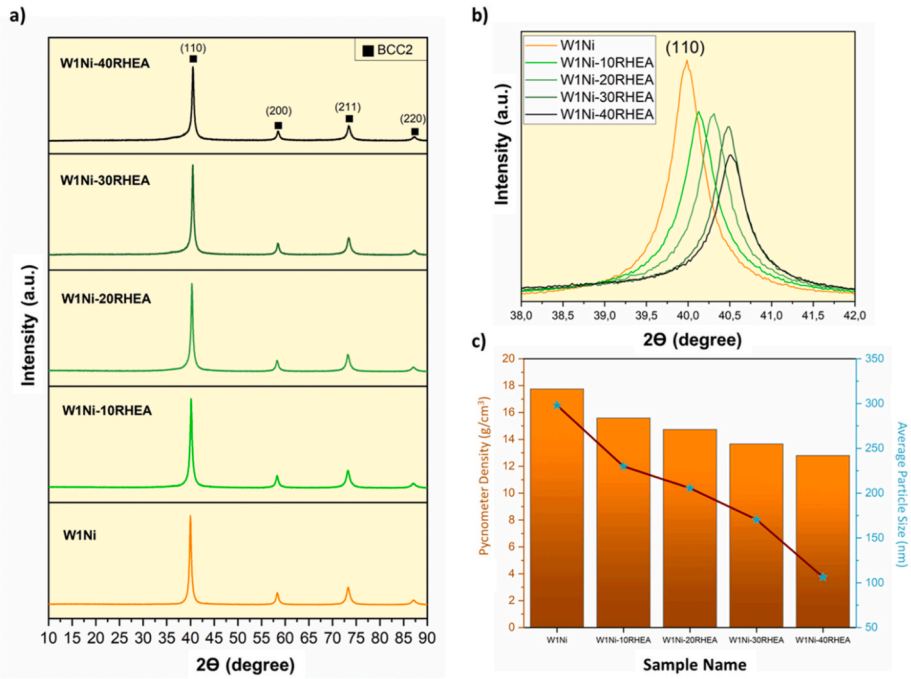

Fig. 4. (a) XRD analysis, (b) the peak shifting of W1Ni and those reinforced with different amounts of RHEA powders, and (c) the pycnometer density versus the average particle size results of the composite powders.

measured as ~17.75 g/cm^3, the 40 wt% addition of RHEA powders reduced the density down to ~12.80 g/cm^3. Also, the average particle size decreased by adding more reinforcement, which is shown in Fig. 4c. Moreover, the lowest particle size was measured as ~106.3 nm.

3.3. Characterization of W1Ni-XRHEA (X = 10, 20, 30, and 40) sintered samples

Kang et al. [50] reported that 6 h MA'ed WNbMoTaV RHEA powders were spark plasma sintered at 1500, 1600, and 1700 °C, and the optimum time for sintering was chosen as 1500 °C. Moreover, Long et al. [56] tried 1500, 1600, and 1700 °C temperatures for the SPS of NbMoTaWVCr RHEA, and decided that the 1500 °C temperature examined the best result. In addition, Peng et al. [49] produced the NbMoTaWV RHEA by SPS (1500 °C and 10 min). Shivakumar et al. [75] proved that Ni was effective as activated sintering for NbMoTaW RHEA, and NbMoTaW-Ni RHEA was sintered at 1800 °C. Furthermore, Qin et al. [66] designed the activated sintering with Ni for TiNbMoTaW-based refractory high-entropy nanoalloys by using SPS (1200–1600 °C for 5 min), then they decided that the 1300 °C temperature was optimum, and could be used for the further experiments. In this study, activated sintering was provided with Ni, and 72 h MA'ed composite powders were spark plasma sintered (SPS'ed) at 1410 °C for 1 min. The SEM images and EDS results of W1Ni and W1Ni-XRHEA composites are shown in Fig. 5a–e. Based on the SEM images, two different regions, according to their colors, were observed as white and grey for all samples. In the general EDS as weight percentage (wt.%), while the Ni amount was stable and around 1 wt%, Nb, Mo, V, and Ta elements amount increased with reinforcement amount. The white region was observed in all samples that are rich for W and, therefore, can be named as Region 1 (Fig. 5a–e). On the other hand, the grey region (Region 2) in the SPS'ed W1Ni sample contains a high amount of Ni (~17 wt%). With the incorporation of increasing RHEA content into the W1Ni sample, the grey regions (Regions 2 in Fig. 5b–e) also revealed Mo, Nb, Ta, W, O, and C with some of them increasing with RHEA addition. According to the XRD results, the white region can be matched with the BCC2 phase. Furthermore, (Ta,Nb)C and (Ta,Nb)O_x phases can be shown in the grey regions. The ratio of elements in the grey region was nearly same with ratio of (Ta,Nb)C phase, and (Ta, Nb)O_x phase. Based on the supplementary information (Fig. S2) that presents the color EDS (for W, Ni, Nb, Mo, V, Ta, O, and C elements) of all SPS'ed samples, W was the dominant element for the white region. However, the amounts of Ta and Nb elements started to increase in the grey region. It can refer to (Ta,Nb)C and (Ta,Nb)O_x phases in the XRD patterns. Liu et al. [81] observed same morphology, and was named this grey area as FCC carbide precipitation phase that have Ta, Nb and C elements.

Fig. 6a shows the XRD patterns of the SPS'ed W1Ni-XRHEA (X = 10, 20, 30, and 40) composites. According to the XRD results, the samples had BCC2 phase (ICSD Card No: 96-900-6496, Bravais lattice: body-centered cubic, a = 0.319 nm), Ni phase (ICSD Card No: 96-210-0650, Bravais lattice: face-centered cubic, a = 0.352 nm), (Ta,Nb)O_x that is the same phase in RHEA powders and (Ta,Nb)C phase (ICSD Card No: 98-000-9891, Bravais lattice: face-centered cubic, a = 0.440 nm). The intensity of (Ta,Nb)O_x and (Ta,Nb)C peaks were very small. Furthermore, it was seen that the Ta and Nb had lower Gibbs free energy based on the thermodynamic calculations (Fig. 2). So, the formation of carbide and oxide of Ta and Nb was expected according to the calculations. Firstly, Genç et al. [92] reported that the activated sintered W composite had Ni phase. In the literature, situations where the Ta_2VO_6 phase exists are frequently encountered. Long et al. [56] observed the Ta_2VO_6 phase for the SPS'ed NbMoTaWVCr HEA. Moreover, Kang et al. [50] showed that the Ta_2VO_6 phase was observed in the SPS'ed WNbMoTaV HEA system. Also, Peng et al. [49] reported the same XRD peaks as a tetragonal precipitate in the SPS'ed NbMoTaWV HEA. The Gibbs free energy of formation between Nb/Ta and C is significantly lower than that of Mo/W and C that come from graphite foil [93]. So, the (Ta,Nb)C phase was observed in this study. Furthermore, Boztemur et al. [52] proved using CALPHAD analysis that the NbC and Ta_2VO_6 structure formation was observed for the WNbMoVTa system in the oxygen and carbon environment. In another study, Liu et al. showed the FCC carbide precipitation phase which included Ta, Nb and C elements due to WC impurity. Moreover, Gu et al. [82] observed (Nb,Ta)C phase results from WC contamination. The Rietveld analyses of these phases versus to the addition of RHEA are shown in Fig. 6b and c. While BCC2 and Ni phase

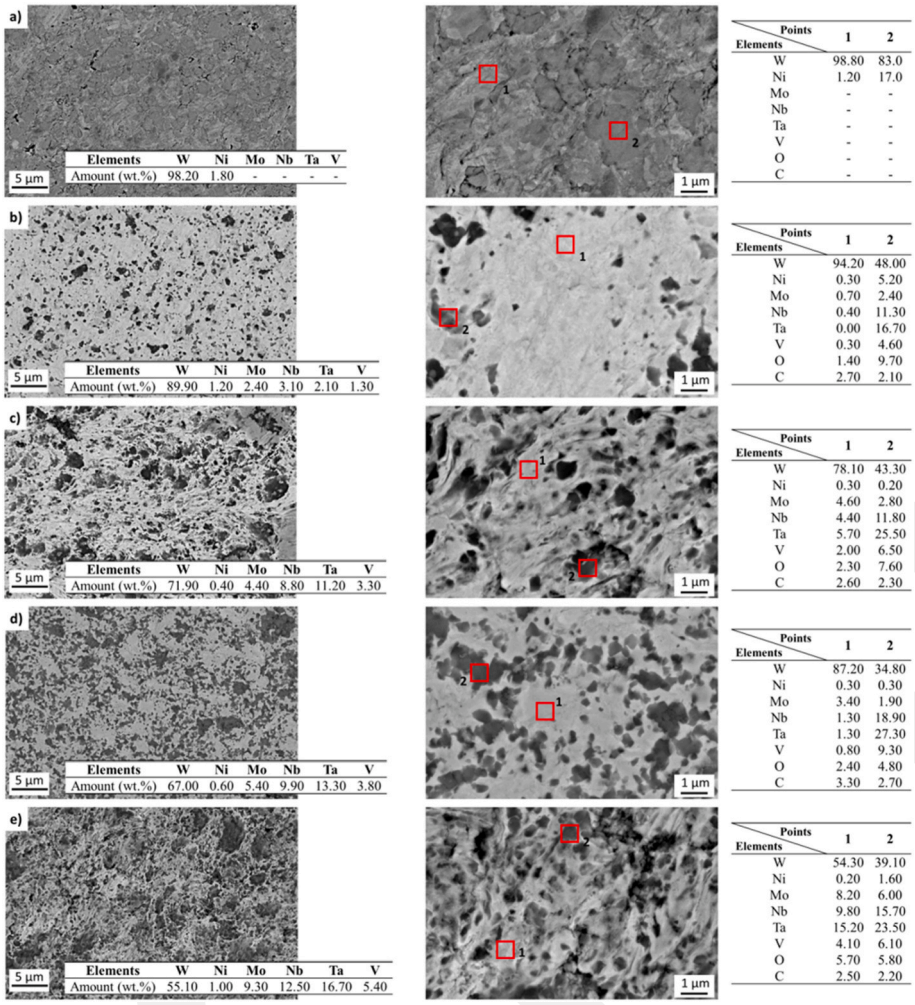

Fig. 5. The SEM images and general/point EDS results of (a) W1Ni, (b) W1Ni-10RHEA, (c) W1Ni-20RHEA, (d) W1Ni-30RHEA and W1Ni-40RHEA sintered samples.

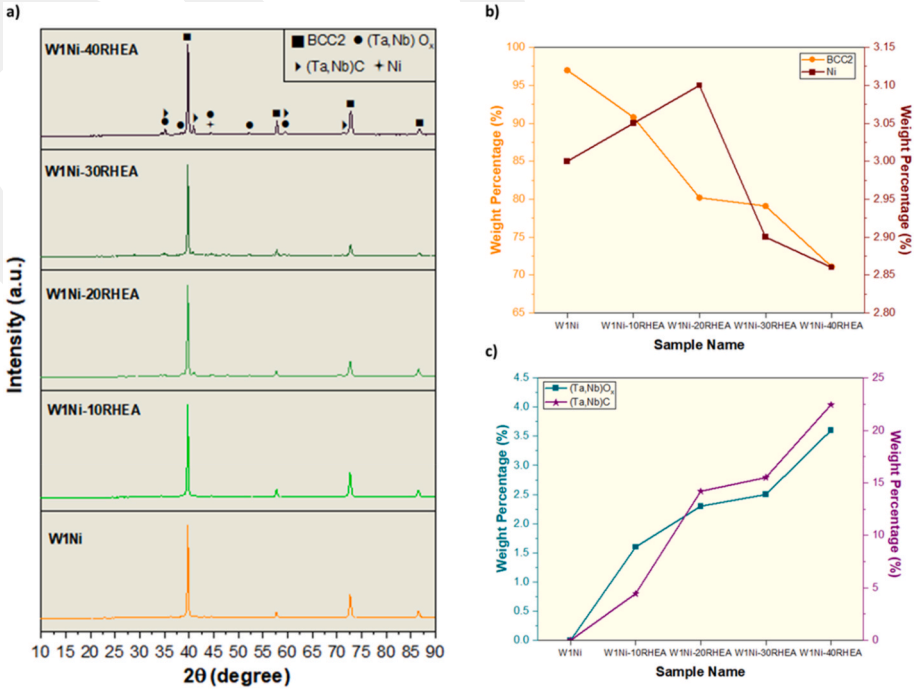

Fig. 6. (a) XRD patterns of the SPS'ed samples, and (b,c) their corresponding Rietveld analysis (weight percentages of the phases for all composites).

amounts are stable, the amount of (Ta,Nb)C and (Ta,Nb)O_x phase increased with increasing reinforcement. It was previously mentioned that RHEA powders contained (Ta,Nb)O_x phase due to the adsorbed oxygen arising from process conditions.

Fig. 7 presents density, Vickers microhardness versus grain size measurements, and wear test results of the MA'ed 6 h and SPS'ed W1Ni, W1Ni-10, 20, 30, and 40RHEA samples. Also, the exact values of these tests are shown in supplementary information (Fig. S3). The spark plasma sintered samples were observed based on Archimedes' density compared to their theoretical density (Fig. 7a). The theoretical density decreased with the increasing amount of reinforcement. Also, the Archimedes' density was decreasing with this trend. However, the different phases were observed in the XRD graphs for the W1Ni-10, 20, 30, and 40RHEA samples. These phases were effective for the theoretical density calculation. So, the difference between theoretical density and Archimedes' density was getting less. As seen in Fig. 7b, the microhardness increased steadily with increasing RHEA additions, from 5.09 GPa for the W1Ni sample to 10.10 GPa for the W1Ni-40RHEA. This is an increase of almost two folds, also revelaed by the corresponding indentation marks getting smaller. The effect of the addition of the RHEA reinforcement to the microhardness value was similar in 20 and 30 wt% of RHEAs. But the obvious increase trend was valid for the 40 wt % RHEA addition. The exact correlation was observed with grain size measurements. Ahmed et al. [18] reported a 7 GPa microhardness value for the SPS'ed WTaVCr alloy. Similarly, Peng et al. [49] reported 7.59 GPa microhardness for the SPS'ed NbMoTaWV RHEA. Further, Long et al. [56] showed that the Cr addition of this NbMoTaWV RHEA increased its microhardness to 10.52 GPa. Although, these results were comparable with this study, the SPS'ed W1Ni-40RHEA sample gave the best result in these alloys. There were some extra phases in the XRD pattern, such as (Ta,Nb)O_x and (Ta,Nb)C. Rudolf [94] mentioned that the hardness of TaC-NbC phases was nearly 7.6 GPa. These phases can be effective on the mechanical properties of samples. The specific wear rate versus the wear volume loss values is shown in Fig. 7c. Based on the graph trend, the best result was obtained with the SPS'ed W1Ni-40RHEA sample. Fig. 7d shows wear depth versus distance values. In the literature, Alvi et al. [48] reported that the CuMoTaWV sample had ~40 $\times 10^{-4}$ mm^3/N.m wear rate and was observed due to formation of Ta and W tribolayer in the wear track.

3.4. The irradiation resistance of sintered samples

After He^+ irradiation, the SEM images ($\times$ 10,000 and $\times$ 160,000 magnifications) and XRD shifting of SPS'ed samples are shown in Fig. 8. Dislocation loops and helium bubbles create, migrate, agglomerate, and expand as a result of irradiating an area with helium ions. The loop expansion is contingent upon both the merging of loops and the absorption of the surrounding irradiation flaws. The absorption of vacancies and helium atoms is what drives the formation of helium bubbles [95]. In addition to serving as a good nucleation site for helium bubbles, the pre-existing dislocation acts as a powerful absorption sink for irradiation flaws. At the later stage of irradiation, the size of helium bubbles is generally bigger in the region close to the dislocation than in the region without dislocation at the same fluence. In other words, fractal features are present in the growth of dendritic structures in fuzz and are mainly caused by two factors: Initially, the dislocation loop formed during the formation of the helium bubble slips to the surface and gets destroyed there. The current formation technique may also provide a satisfactory explanation for the experiment's reported lack of preferential development axes in the fuzz. Second, helium bubbles rise to the surface as a result of surface stress during the growth phase [96,97]. These formations are generally seen in plasma-facing materials. Huang et al. [98] applied 10–30 min irradiation to pure tungsten and showed the wavy structure as much as the same with this study. Moreover, Pu et al. [99] mentioned that the RHEA (TaTiNbZr) film produces diverse outcomes, indicating the occurrence of fuzz phenomena on the surface of tungsten stacks when exposed to a broad range of high-energy plasma and elevated irradiation temperatures. Also, Cui et al. [28] reported the same fuzzy structure for pure tungsten after 30 min irradiation. The same fuzz formation was observed with the W1Ni sample (Fig. 8a). This structure transformed to cluster with the addition of 10 wt% RHEA into W1Ni matrix. This deformation was decreased by the W1Ni-20RHEA

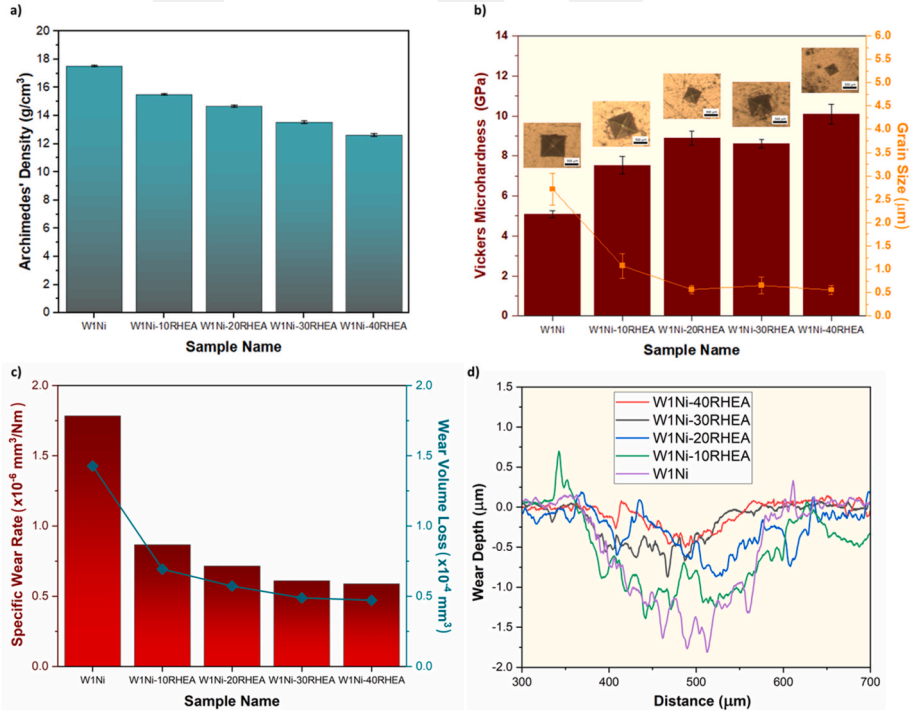

Fig. 7. The SPS'ed samples behavior according to (a) the Archimedes' density, (b) the Vickers microhardness with the indentation trace versus grain size measurements, (c) the specific wear rate versus the wear volume loss, and (d) the wear profile graph.

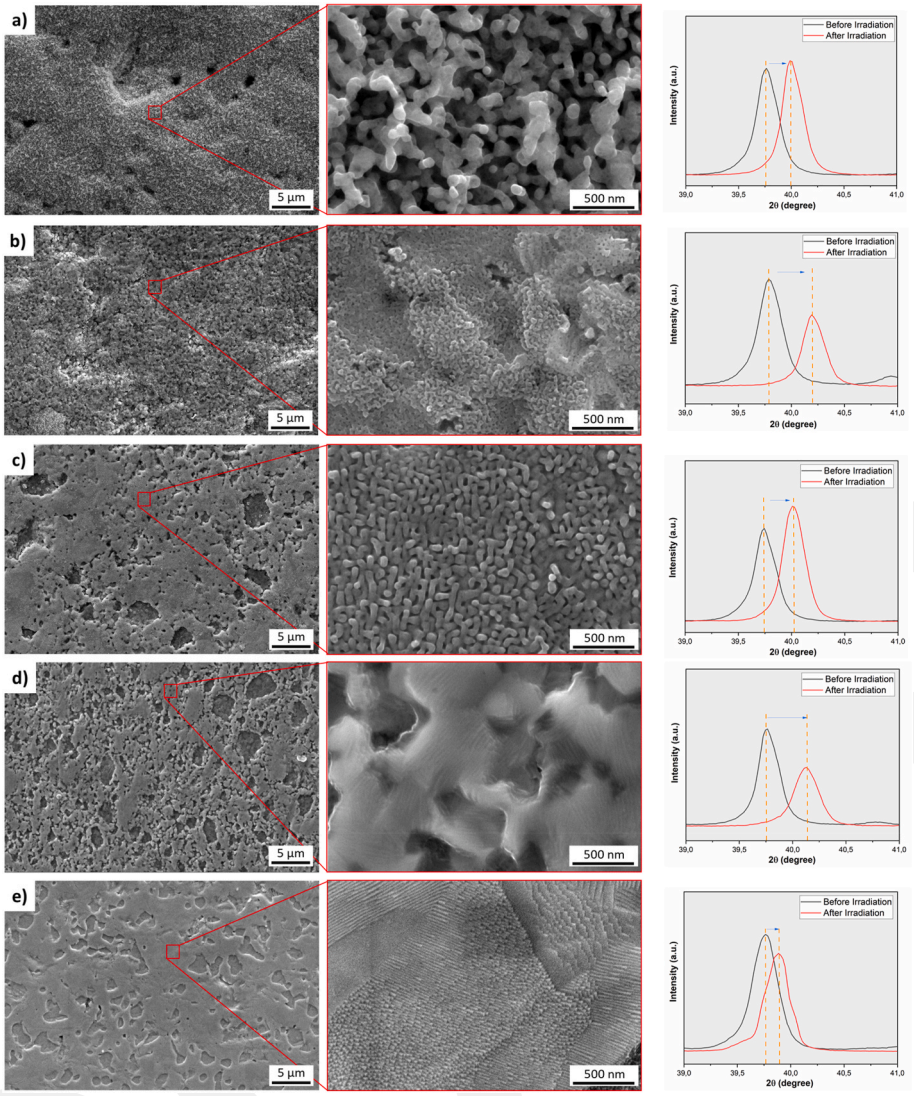

Fig. 8. The SEM images (× 10,000 and × 160,000 magnifications) and XRD shifting of (a) W1Ni, (b) W1Ni-10RHEA, (c) W1Ni-20RHEA, (d) W1Ni-30RHEA, and (e) W1Ni-40RHEA SPS'ed samples after He^+ irradiation.

SPS'ed sample, and He^+ bubbles [96,100] are placed under the surface after He^+ irradiation and create a wavy structure [98]. Although, the failure that depends on the helium was enhanced, the cracks were still present. These cracks were investigated with the W1Ni-30RHEA sample, and the wavy formation was obtained. However, the SPS'ed W1Ni-40RHEA sample showed the best surface stability. According to Cheng et al. [101], the CrMoTaWV RHEA has an astonishing 8.9 times slower development rate of fuzz than W, in addition to displaying a fuzz structure formation fluence that is 20 times higher. Moreover, Cui et al. [43] obtained the higher surface stability for $W_{70}(TaVCrTi)_{30}$ alloy between 10, 20, 30, and 40 wt% reinforcement amounts. Also, the XRD peak shifting shows different properties based on the irradiation amount. The lattice expansion of irradiated alloys may be aided by the defects (associated clusters, point defects, and dislocation loops), micro-strain, and flaws in the lattice structure brought on by ion irradiation [102].

Because of the high grain boundary density it can create, grain size refinement is suggested as a way to improve radiation tolerance in materials under extreme irradiation conditions [103]. It is also hypothesized that grain boundaries, which serve as sinks for defects and particles (such as helium), will accelerate vacancy-interstitial annihilation. This may result in a reduction of defect density (such as voids, bubbles, and interstitial clusters) and an increase in the microstructure's resistance to radiation [104]. The ultrafine grain structure plays an important role in improving surface stability. Moreover, this better surface stability provides a self-healing mechanism [43]. Fig. 9 shows the cross-sectional SEM images and the point EDS results from the irradiated and unirradiated parts of composites. According to the grain size measurements (Fig. 7b), the higher grain sizes were measured on the fracture surface for the SPS'ed W1Ni sample. Based on the literature research [104,105], bigger grain sizes affect that helium bubbles can infuse easily into the surface. So, the thickness of the irradiated part was the highest in the W1Ni sample. The addition of RHEA into W1Ni matrix, the grain size was going to decrease, and the irradiated part of surface started to be thin. The best surface stability was obtained with the W1Ni-40RHEA sample, and provided the self-healing mechanism. Based on the regional EDS results, a higher amount of C and O elements were detected on the irradiated surface. Also, the changing of W amount between the top and bottom was nearly 40 % and was higher on the surface for the SPS'ed W1Ni sample. However, this value decreased to 1 % for the W1Ni-40RHEA sample. This change can be explained with the thermodynamics. Based on the calculations (Fig. 2), the loss of W was eliminated with RHEA addition. The oxide layer provided the protection of the W matrix. Helium bubbles placed under the surface after irradiation cause the surface hardening and create defects and vacancies in the crystal structure. So, the microhardness values of samples increase after

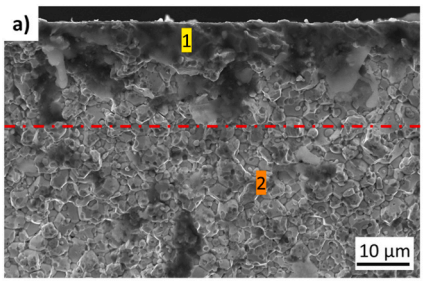

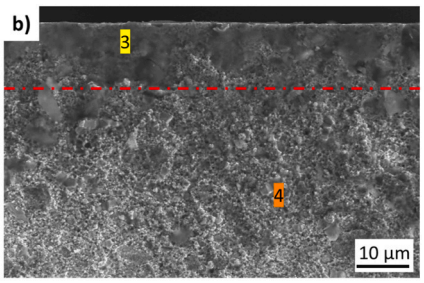

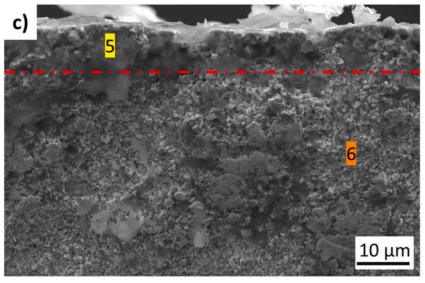

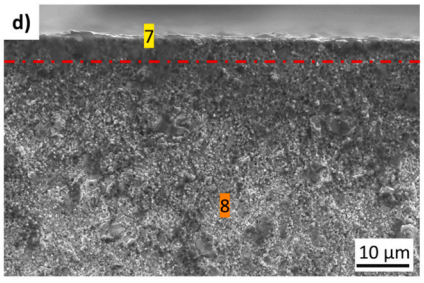

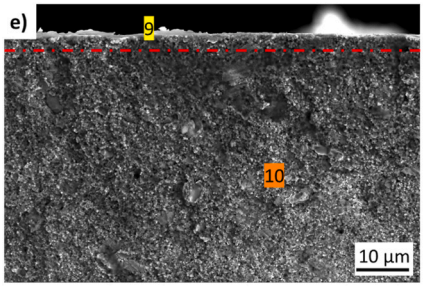

Points \ Elements (wt.%)	W	Ni	Mo	Nb	Ta	V	O	C
1	66.00	1.50	-	-	-	-	10.10	22.40
2	92.90	1.50	-	-	-	-	2.80	2.80
3	51.60	4.50	3.00	4.20	11.30	1.80	10.10	13.50
4	76.30	1.90	1.60	2.70	11.90	1.70	2.30	2.50
5	54.20	1.40	2.90	1.80	1.80	0.80	16.00	21.10
6	75.90	1.20	2.90	3.70	5.60	1.50	4.60	4.60
7	51.20	1.00	4.90	8.10	11.60	3.40	9.70	10.10
8	59.10	0.90	5.20	8.50	15.60	3.50	3.60	3.70
9	53.50	1.10	5.40	6.70	14.30	3.50	6.60	8.90
10	54.20	1.10	7.00	8.20	17.60	4.40	4.30	3.20

Fig. 9. The cross-sectional SEM images at × 5000 magnification and point EDS results of (a) W1Ni, (b) W1Ni-10RHEA, (c) W1Ni-20RHEA, (d) W1Ni-30RHEA, and (e) W1Ni-40RHEA SPS'ed samples after He^+ irradiation.

helium implementation. In the literature, Atwani et al. [106] analyzed the hardness test results of the helium irradiated WTaCrVHf RHEA film and noticed that hardness of the RHEA increased by helium irradiation. Then, this situation can be explained by two additional factors. Firstly, there may be changes in hardness due to material homogenization resulting from the shift from an ordered to a disordered state, leading to increased lattice distortion. Secondly, the irradiation with heavy ions can lead to a refinement of grain size in this RHEA, as previously demonstrated and illustrated. Since the hardness is influenced by the grain size according to a power law relationship, even a slight refinement in grain size can lead to a significant change in hardness. This effect becomes more pronounced when the grain size is extremely small, approaching the threshold between the Hall-Petch and Inverse Hall-Petch phenomena [106]. In another study, Moschetti et al. [107] mentioned that TiZrNbHfTa alloy showed an increment in hardness after irradiation, which is attributed to classic radiation hardening due to defect formation in the lattice. Waseem et al. [108] showed that the microhardness value of $W_{0.5}(TaTiVCr)_{0.5}$ multi-component alloy increased from 11.6 GPa to 14.9 GPa after He^+ irradiation. These same cases were observed in this study. After irradiation, it can be said that, as the amount of RHEAs is increased, the hardness values rise as well. Table 1 shows the hardness of irradiated sample values and the percentage difference in the unirradiated sample. After irradiation, hardness values are increased from 5.47 GPa to 10.53 GPa.While the SPS'ed W1Ni hardness value increased by 7.47 %, the SPS'ed W1Ni-10RHEA sample hardness increased by 11.39 %. Moreover, SPS'ed W1Ni-20RHEA and W1Ni-30RHEA hardness values increased by 9.43 % and 9.37 %, respectively. Finally, W1Ni-40RHEA sample hardness changed and increased by 4.26 % after irradiation. After these examinations, it was observed that the sample with the highest percentage increase in hardness value after radiation was W1Ni-10RHEA. In the case of 20 wt%, 30 wt%, and 40 wt% RHEA addition, the percentage increment in the hardness value is gradually decreasing. The least increment was obtained with the W1Ni-40RHEA SPS'ed sample. However, due to the need of reducing neutron activation, elements in our system may be substitued by V, Ta, W in future studies. Nb and Ni could be limited usage among the neutron activation elements for fusion reactor materials [109].

Table 1
Microhardness values of the SPS'ed samples after irradiation and microhardness increment percentages.

Sample Name	Microhardness Value After Irradiation (GPa)	Microhardness Change (%)
W1Ni	5.47 ± 0.62	7.47
W1Ni-10RHEA	8.39 ± 0.58	11.39
W1Ni-20RHEA	9.74 ± 0.45	9.43
W1Ni-30RHEA	9.42 ± 0.54	9.37
W1Ni-40RHEA	10.53 ± 0.65	4.26

4. Conclusions

This study presents the results of the mechanical and Helium irradiation behavior of the W1Ni-XRHEA (X = 10, 20, 30, and 40) system.

The mechanical alloying and annealing were used for the production of the high crystallinity and ultra-fine RHEA powders. These RHEA powders were used for reinforcement into W1Ni pre-alloyed powders. This reinforcement provided higher strength and helium irradiation resistance. The activated sintering, in which Ni element was used as an aid, was realized by spark plasma sintering. The main conclusions can be summarized as follows:

- Nb-Mo-V-Ta elements were mechanically alloyed for different hours in order to create single-phase BCC structure. 6 h MA'ed single-phase NbMoVTa RHEA powders were annealed for increasing the crystallinity. BCC1 phase was obtained after milling, and $(Ta_2,Nb)O_x$ phase was seen after annealing because of oxygen.
- 72 h pre-alloyed W1Ni powders were used as matrix, and were reinforced with 10, 20, 30, 40 wt% RHEA powders. After milling, the peak shifting to the right was observed with increasing reinforcement amount. This correlation was detected for the particle size and the decrease in pycnometer density.
- Based on the XRD graphs, BCC2, (Ta,Nb)C, Ni, and $(Ta,Nb)O_x$ phases were observed after the sintering process. While the amounts of Ni and BCC2 phases stayed stable, the amounts of (Ta,Nb)C and $(Ta,Nb)O_x$ phases increased with the higher reinforcement addition. Among all sintered samples, the highest amounts of (Ta,Nb)C and $(Ta,Nb)O_x$ phases were respectively found as 22.44 and 3.6 wt% for the W1Ni-40RHEA sample.
- The microhardness value of the SPS'ed W1Ni sample was measured as 5.09 GPa, and this value increased to 10.10 GPa for the SPS'ed W1Ni-40RHEA sample. Grain size decreased to ~0.56 μm (W1Ni-40RHEA) from ~2.72 μm (W1Ni). Based on the specific wear rate and wear volume loss graph trend, the best result was obtained with the SPS'ed W1Ni-40RHEA composite.
- The helium irradiation deformed W1Ni sample highly. The addition of 40 wt% RHEA into W1Ni was enhanced to irradiation behavior of tungsten. While the fuzzy structure was observed in the W1Ni sample, this structure transformed to the wavy morphology in the W1Ni-40RHEA sample. Moreover, the thin layer was detected for the irradiated part for the cross-sectional layer. The microhardness value rose to nearly 4.26 % after irradiation. This amount was the minimum for the W1Ni-40RHEA composite.

CRediT authorship contribution statement

Burçak Boztemur: Writing – original draft, Investigation, Formal analysis, Conceptualization. **Kaan Filiz:** Writing – review & editing, Formal analysis. **Zahide Karagüney:** Writing – review & editing, Formal analysis. **Eyüpcan Gökaydın:** Writing – review & editing, Formal analysis. **Yasin Bozkurt:** Writing – review & editing, Formal analysis. **Ceren Özbasmacı:** Writing – review & editing, Formal analysis. **Kübra Gürcan Bayrak:** Formal analysis. **Yue Xu:** Formal analysis. **Laima Luo:** Formal analysis. **Duygu Ağaoğulları:** Writing – original draft, Supervision, Project administration, Conceptualization. **M. Lütfi Öveçoğlu:** Writing – original draft, Conceptualization.

Notes

The authors declare no competing financial interest.

Declaration of competing interest

The authors declare that they have no known competing financial interests or personal relationships that could have appeared to influence the work reported in this paper.

Acknowledgment

This work was financially supported by the Scientific Research Projects Department of Istanbul Technical University with the project number of MGA-2024-45483. Also, the optimization of refractory high entropy alloys was conducted within the scope of the 119M980 project supported by the Scientific and Technological Research Council of Türkiye (TUBITAK). The authors thank Mertcan Kaba and Prof. Dr. Hüseyin Çimenoğlu for their help in conducting wear tests in the Mechanical Metallurgy Laboratories at Istanbul Technical University. The authors also thank Mustafa Dolkan and Hakan Arslan for their help in wire erosion cutting.

Appendix A. Supplementary data

Supplementary data to this article can be found online at https://doi.org/10.1016/j.intermet.2024.108621.

Data availability

Data will be made available on request.

References

[1] J. Ongena, G. Van Oost, Energy for future centuries Will fusion be an inexhaustible, safe and clean energy source? Fusion Sci. Technol. 41 (2002) 3–14, https://doi.org/10.13182/fst02-a11963498.
[2] K. Łukasiewicz, P. Pietrzak, J. Kraciuk, E. Kacperska, M. Cieciora, Sustainable energy development—a systematic literature review, Energies 15 (2022), https://doi.org/10.3390/en15218284.
[3] G. Dubus, From Plain visualisation to vibration sensing: using a camera to control the flexibilities in the ITER remote handling equipment (doctoral dissertation). https://www.researchgate.net/publication/270897032, 2014.
[4] B.W. Brook, A. Alonso, D.A. Meneley, J. Misak, T. Blees, J.B. van Erp, Why nuclear energy is sustainable and has to be part of the energy mix, Sustain. Mater. Technol. 1 (2014) 8–16, https://doi.org/10.1016/j.susmat.2014.11.001.
[5] S. Saenko, A. Vladimir, V.K. Ivanov, Anatoly F. Tsyb, Tatjana I. Bogdanova, Mykolo Tronko, Yuryi U. Demidchik, Yamashita, The Chernobyl Accident and its Consequences, vol. 23, 2011, pp. 234–243.
[6] A.M. Bradshaw, T. Hamacher, U. Fischer, Is nuclear fusion a sustainable energy form? Fusion Eng. Des. 86 (2011) 2770–2773, https://doi.org/10.1016/j.fusengdes.2010.11.040.
[7] J. Winter, G. Gebauer, Dust in magnetic confinement fusion devices and its impact on plasma operation, J. Nucl. Mater. 266 (1999) 228–233, https://doi.org/10.1016/S0022-3115(98)00526-1.
[8] D.M. Duffy, Modeling plasma facing materials for fusion power, Mater. Today 12 (2009) 38–44, https://doi.org/10.1016/S1369-7021(09)70297-4.
[9] H. Bolt, A. Brendel, D. Levchuk, H. Greuner, H. Maier, Materials for plasma facing components of fusion reactors, Energy Mater 1 (2006) 121–126, https://doi.org/10.1179/174892406x144451.
[10] Ch Linsmeier, M. Rieth, J. Aktaa, T. Chikada, A. Hoffmann, J. Hoffmann, A. Houben, H. Kurishita, X. Jin, M. Li, A. Litnovsky, S. Matsuo, A. von Müller, V. Nikolic, T. Palacios, R. Pippan, D. Qu, J. Reiser, J. Riesch, T. Shikama, R. Stieglitz, T. Weber, S. Wurster, J.-H. You, Z. Zhou, 1, Development of advanced high heat flux and plasma-facing materials, Nucl. Fusion 57 (2017) 092007.
[11] J. Linke, J. Du, T. Loewenhoff, G. Pintsuk, B. Spilker, I. Steudel, M. Wirtz, Challenges for plasma-facing components in nuclear fusion, Matter Radiat. Extremes 4 (2019), https://doi.org/10.1063/1.5090100.
[12] M. Ulrickson, V. Barabash, S. Chiocchio, G. Federici, G. Janeschitz, R. Matera, M. Akiba, G. Vieider, C. Wu, I. Mazul, Selection of plasma facing materials for ITER, Proc. - Symp. Fusion Eng. 1 (1995) 394–398, https://doi.org/10.1109/fusion.1995.534250.
[13] C.L. Briant, The properties and uses of refractory metals and their, ALLOYS 322 (1994) 305–314.
[14] T. Brown, P. Pitfield, Tungsten, Crit. Met. Handb, 2014 67171.
[15] S. Nogami, I. Ozawa, D. Asami, N. Matsuta, S. Nakabayashi, S. Baumgärtner, P. Lied, K. Yabuuchi, T. Miyazawa, Y. Kikuchi, M. Wirtz, M. Rieth, A. Hasegawa, Tungsten–tantalum alloys for fusion reactor applications, J. Nucl. Mater. 566 (2022) 153740, https://doi.org/10.1016/j.jnucmat.2022.153740.
[16] J.W. Coenen, J. Riesch, J.-H. You, H. Gietl, T. Hoeschen, R. Neu, B. Jasper, Y. Mao, A. Terra, C. Linsmeier, S. Sree, C. Broeckmann, Tungsten composite materials for fusion first wall applications, in: 26th IAEA Fusion Energy Conf., 2018, p. 806. https://nucleus.iaea.org/sites/fusionportal/SharedDocuments/FEC2016/fec2016-preprints/preprint0085.pdf.
[17] R. Martins, J.B. Correia, P. Czarkowski, R. Miklaszewski, A. Malaquias, R. Mateus, E. Alves, M. Dias, Irradiation damage on CrNbTaVWx high entropy alloys, Nucl. Instrum. Methods Phys. Res. B. 538 (2023) 212–217, https://doi.org/10.1016/j.nimb.2023.03.010.
[18] O. Ahmed, J. Lee, H. Mo, H. Jin, The effect of Ti on the sintering and mechanical properties of refractory high-entropy alloy Ti x WTaVCr fabricated via spark plasma sintering for fusion plasma-facing materials, Mater. Chem. Phys. 210 (2018) 87–94, https://doi.org/10.1016/j.matchemphys.2017.06.054.

[19] Y. Oh, N. Kwak, K. Lee, W.-S. Ko, H.N. Han, Ductility enhancement of tungsten after plastic deformation, J. Alloys Compd. 787 (2019) 801–814, https://doi.org/10.1016/j.jallcom.2019.02.097.

[20] J.-H. You, A review on two previous divertor target concepts for DEMO: mutual impact between structural design requirements and materials performance, Nucl. Fusion 55 (2015) 113026.

[21] M.A. Umer, D. Lee, O.A. Waseem, H.J. Ryu, S.H. Hong, Fabrication of protective-coated SiC reinforced tungsten matrix composites with reduced reaction phases by spark plasma sintering, Met. Mater. Int. 22 (2016) 493–500, https://doi.org/10.1007/s12540-016-5700-y.

[22] R.A. Pitts, S. Carpentier, F. Escourbiac, T. Hirai, V. Komarov, S. Lisgo, A. S. Kukushkin, A. Loarte, M. Merola, A.S. Naik, R. Mitteau, M. Sugihara, B. Bazylev, P.C. Stangeby, A full tungsten divertor for ITER : physics issues and design status, J. Nucl. Mater. 438 (2013) 48–56, https://doi.org/10.1016/j.jnucmat.2013.01.008.

[23] O. El-Atwani, N. Li, M. Li, A. Devaraj, J.K.S. Baldwin, M.M. Schneider, D. Sobieraj, J.S. Wróbel, D. Nguyen-Manh, S.A. Maloy, E. Martinez, Outstanding radiation resistance of tungsten-based high-entropy alloys, Sci. Adv. 5 (2019) 1–10, https://doi.org/10.1126/sciadv.aav2002.

[24] B. Yu, D. Zhu, C. Li, C. Xuan, R. Ding, B. Gao, J. Chen, C. Du, Characterization of the peak temperature on upper W divertor target during D and He plasma discharges in EAST, Nucl. Mater. Energy. 34 (2023) 101362, https://doi.org/10.1016/j.nme.2023.101362.

[25] Y. Oya, N. Inozume, Y. Hoshino, N. Yoshida, T. Hinoki, K. Yabuuchi, Y. Hatano, Q. Zhou, F. Sun, R. Kolasinski, C.N. Taylor, M. Shimada, Thermal annealing effect on D retention for damaged W-10%Re alloy, Fusion Eng. Des. 196 (2023) 113981, https://doi.org/10.1016/j.fusengdes.2023.113981.

[26] K. Arshad, M.-Y. Zhao, Y. Yuan, Y. Zhang, Z.-H. Zhao, B. Wang, Z.-J. Zhou, G.-H. Lu, Effects of vanadium concentration on the densification, microstructures and mechanical properties of tungsten vanadium alloys, J. Nucl. Mater. 455 (2014) 96–100, https://doi.org/10.1016/j.jnucmat.2014.04.019.

[27] N. Kwak, S. Kang, G. Min, R. Arredondo, K. Jeong, H. Kim, T. Schwarz-selinger, M. Balden, A. Manhard, J. You, H. Nam, Bimodal structured chromium-tungsten composite as plasma-facing materials : sinterability, mechanical properties, and deuterium retention assessment, Acta Mater. 262 (2024) 119453, https://doi.org/10.1016/j.actamat.2023.119453.

[28] H. Cui, N. Liu, L. Luo, Y. Xu, J. Cheng, Y. Wu, A prospect of using ternary W-5 wt %V-5 wt%Ta alloy manufactured by mechanical alloying and spark plasma sintering as plasma-facing material, J. Alloys Compd. 903 (2022) 163899, https://doi.org/10.1016/j.jallcom.2022.163899.

[29] B.S. Murty, J.W. Yeh, S. Ranganathan, P.P. Bhattacharjee, 1 - a brief history of alloys and the birth of high-entropy alloys, in: High-Entropy Alloy, second ed., Elsevier, 2019, pp. 1–12, https://doi.org/10.1016/B978-0-12-816067-1.00001-1.

[30] N.I.M. Nadzri, A. Khemar, J.A. Wahab, M.M. Mahat, High entropy alloy towards functional materials application : a review high entropy alloy towards functional materials application : a review, J. Phys. Conf. Ser. 2169 (2022) 012007, https://doi.org/10.1088/1742-6596/2169/1/012007.

[31] B.S. Murty, J.W. Yeh, S. Ranganathan, P.P. Bhattacharjee, Applications and future directions, high-entropy alloy, 247–257, https://doi.org/10.1016/b978-0-12-816067-1.00013-8, 2019.

[32] Y. sheng Tian, W. zhe Zhou, Q. biao Tan, M. xu Wu, S. Qiao, G. liang Zhu, A. ping Dong, D. Shu, B. de Sun, A review of refractory high-entropy alloys, Trans. Nonferrous Met. Soc. China (English Ed. 32 (2022) 3487–3515, https://doi.org/10.1016/S1003-6326(22)66035-7.

[33] S. Kumar, A. Linda, Y. Shadangi, V. Jindal, Influence of micro-segregation on the microstructure, and microhardness of MoNbTaxTi(1-x)W refractory high entropy alloys: experimental and DFT approach, Intermetallics 164 (2024) 108080, https://doi.org/10.1016/j.intermet.2023.108080.

[34] V.K. Pandey, Y. Shadangi, V. Shivam, B.N. Sarma, N.K. Mukhopadhyay, Theoretical and experimental study on phase stability of TiVZrMoW refractory high entropy alloy, Philos. Mag. A 102 (2022) 480–503, https://doi.org/10.1080/14786435.2021.2001066.

[35] E.P. George, W.A. Curtin, C.C. Tasan, High entropy alloys: a focused review of mechanical properties and deformation mechanisms, Acta Mater. 188 (2020) 435–474, https://doi.org/10.1016/j.actamat.2019.12.015.

[36] D.B. Miracle, O.N. Senkov, A critical review of high entropy alloys and related concepts, Acta Mater. 122 (2017) 448–511, https://doi.org/10.1016/j.actamat.2016.08.081.

[37] W. Xiong, A.X.Y. Guo, S. Zhan, C. Liu, S. Cecilia, Refractory high-entropy alloys : a focused review of preparation methods and properties, J. Mater. Sci. Technol. 142 (2023) 196–215, https://doi.org/10.1016/j.jmst.2022.08.046.

[38] M. Wang, Y. Lu, J. Lan, T. Wang, C. Zhang, Z. Cao, T. Li, P.K. Liaw, Lightweight, ultrastrong and high thermal-stable eutectic high-entropy alloys for elevated-temperature applications, Acta Mater. 248 (2023) 118806, https://doi.org/10.1016/j.actamat.2023.118806.

[39] D. Kalita, Y. Zhang, K. Mulewska, W. Chrominski, Y. Ge, W.L. Boldman, P. D. Rack, Y. Wang, W.J. Weber, J. Jagielski, The microstructure and He + ion irradiation behavior of novel low-activation W-Ta-Cr-V refractory high entropy alloy for nuclear applications, Nucl. Mater. Energy. 37 (2023) 101513, https://doi.org/10.1016/j.nme.2023.101513.

[40] Q. Xu, X. Yuan, J. Eckert, D. Şopu, Crack-healing mechanisms in high-entropy alloys under ion irradiation, Acta Mater. 263 (2024) 119488, https://doi.org/10.1016/j.actamat.2023.119488.

[41] S. qin Xia, Z. Wang, T. fei Yang, Y. Zhang, Irradiation behavior in high entropy alloys, J. Iron Steel Res. Int. 22 (2015) 879–884, https://doi.org/10.1016/S1006-706X(15)30084-4.

[42] B.S. Murty, J.W. Yeh, S. Ranganathan, Applications and future directions, in: High Entropy Alloy, Elsevier, 2014, pp. 159–169, https://doi.org/10.1016/B978-0-12-800251-3.00010-9.

[43] H. Cui, N. Liu, L. Luo, Y. Xu, J. Cheng, Y. Wu, Behavior of high-entropy W-rich alloys Wx(TaVCrTi)y under He+ irradiation, Fusion Eng. Des. 172 (2021) 112904, https://doi.org/10.1016/j.fusengdes.2021.112904.

[44] O.A. Waseem, H.J. Ryu, Powder Metallurgy processing of a Wx TaTiVCr high-entropy alloy and its derivative alloys for fusion material applications, Sci. Rep. 7 (2017) 1–14, https://doi.org/10.1038/s41598-017-02168-3.

[45] O.N. Senkov, G.B. Wilks, D.B. Miracle, C.P. Chuang, P.K. Liaw, Refractory high-entropy alloys, Intermetallics 18 (9) (2010) 1758–1765, https://doi.org/10.1016/j.intermet.2010.05.014.

[46] T. Nagase, M. Takemura, M. Matsumuro, T. Maruyama, Solidification Microstructure of AlCoCrFeNi2.1 Eutectic High Entropy Alloy Ingots*, 2017, pp. 1–10.

[47] B.F. Coll, D.M. Sanders, Design of vacuum arc-based sources, Surf. Coating. Technol. 81 (1996) 42–51.

[48] S. Alvi, F. Akhtar, High temperature tribology of CuMoTaWV high entropy alloy, Wear 426–427 (2019) 412–419, https://doi.org/10.1016/j.wear.2018.12.085.

[49] H. Peng, Z. Kang, Y. Long, L. Zhou, A two-phase ultrafine-grained NbMoTaWV refractory high entropy alloy with prominent compressive properties, Vacuum 199 (2022) 110930, https://doi.org/10.1016/j.vacuum.2022.110930.

[50] B. Kang, J. Lee, H.J. Ryu, S.H. Hong, Ultra-high strength WNbMoTaV high-entropy alloys with fine grain structure fabricated by powder metallurgical process, Mater. Sci. Eng. 712 (2018) 616–624, https://doi.org/10.1016/j.msea.2017.12.021.

[51] Ö.U. Demirkan, A. Genç, M. Lüt, Effects of Al 2 O 3 addition on the microstructure and properties of Ni activated sintered W matrix composites, Int. J. Refract. Metals Hard Mater. 32 (2012) 33–38, https://doi.org/10.1016/j.ijrmhm.2012.01.004.

[52] B. Boztemur, K.G. Bayrak, H. Gökçe, E. Ayas, Ö. Balcı-Çağıran, B. Derin, D. Ağaoğulları, M.L. Öveçoğlu, Mechanically alloyed and spark plasma sintered WNbMoVTa refractory high entropy alloys: effects of Cr and Al on the microstructural and mechanical properties, J. Alloys Compd. 965 (2023) 171415, https://doi.org/10.1016/j.jallcom.2023.171415.

[53] D. Ağaoğulları, Ö. Balcı, H. Gökçe, M.L. Öveçoğlu, İ. Duman, Comparative investigations of the activated sintered W – 1 wt .% Ni composites reinforced with various oxide and boride particles, J. Refract. Met. Hard Mater. 41 (2013) 577–584, https://doi.org/10.1016/j.ijrmhm.2013.07.010.

[54] H. Zhang, Y. Zhao, S. Huang, S. Zhu, F. Wang, D. Li, Manufacturing and analysis of high-performance refractory high-entropy alloy via selective laser melting (SLM), Materials 12 (2019), https://doi.org/10.3390/ma12050720.

[55] B. Kang, J. Lee, H.J. Ryu, S.H. Hong, Ultra-high strength WNbMoTaV high-entropy alloys with fine grain structure fabricated by powder metallurgical process, Mater. Sci. Eng. 712 (2018) 616–624, https://doi.org/10.1016/j.msea.2017.12.021.

[56] Y. Long, X. Liang, K. Su, H. Peng, X. Li, A fine-grained NbMoTaWVCr refractory high-entropy alloy with ultra-high strength: microstructural evolution and mechanical properties, J. Alloys Compd. 780 (2019) 607–617, https://doi.org/10.1016/j.jallcom.2018.11.318.

[57] C. Zhu, Z. Li, C. Hong, P. Dai, J. Chen, Microstructure and mechanical properties of the TiZrNbMoTa refractory high-entropy alloy produced by mechanical alloying and spark plasma sintering, Int. J. Refract. Met. Hard Mater. 93 (2020) 105357, https://doi.org/10.1016/j.ijrmhm.2020.105357.

[58] Y. Long, K. Su, J. Zhang, X. Liang, H. Peng, X. Li, Enhanced strength of a mechanical alloyed NbMoTaWVTi refractory high entropy alloy, Materials 11 (2018) 1–8, https://doi.org/10.3390/ma11050669.

[59] J. Hee, R. Hidayati, S. Jung, Y. Adeyemi, H. Kim, J. Hyun, J. Rhyee, Enhancement of critical current density and strong vortex pinning in synthesized by spark plasma sintering, Acta Mater. 232 (2022) 117971, https://doi.org/10.1016/j.actamat.2022.117971.

[60] L. Van Duong, N. Quoc, N. Ngoc, D. Quoc, Microstructure , mechanical properties , and corrosion behavior of TiVNbZrHf high entropy alloys fabricated by multi-step spark plasma sintering, Int. J. Refract. Met. Hard Mater. 119 (2024) 106529, https://doi.org/10.1016/j.ijrmhm.2023.106529.

[61] I.J. Toth, N.A. Lockington, The kinetics of metallic activation sintering of tungsten, J. Less Common Met. 12 (1967) 353–365, https://doi.org/10.1016/0022-5088(67)90003-3.

[62] G. V Samsonov, V.I. Yakovlev, Activation of the sintering of tungsten by the iron-group metals, Sov, Powder Metall. Met. Ceram. 8 (1969) 804–808, https://doi.org/10.1007/BF00778338.

[63] P.E. Zovas, R.M. German, K.S. Hwang, C.J. Li, Activated and liquid-phase sintering-progress and problems, JOM J. Miner. Met. Mater. Soc. 35 (1983) 28–33, https://doi.org/10.1007/BF03338181.

[64] K.S. Mohammed, A. Rahmat, The role of the activator rich-W interboundary layer on liquid phase sintering of W-pre-alloy bronze composites of Fe and Co additions, Int. J. Refract. Met. Hard Mater. 35 (2012) 170–177, https://doi.org/10.1016/j.ijrmhm.2012.04.016.

[65] J.L. Johnson, Enhanced sintering of tungsten, Int. J. Refract. Met. Hard Mater. 110 (2023) 106017, https://doi.org/10.1016/j.ijrmhm.2022.106017.

[66] M. Qin, S. Shivakumar, J. Luo, Refractory high-entropy nanoalloys with exceptional high-temperature stability and enhanced sinterability, J. Mater. Sci. 58 (2023) 8548–8562, https://doi.org/10.1007/s10853-023-08535-y.

[67] Z.L. Lu, L.M. Luo, J.B. Chen, X.M. Huang, J.G. Cheng, Y.C. Wu, Fabrication of W-Cu/CeO2 composites with excellent electric conductivity and high strength

prepared from copper-coated tungsten and Ceria powders, Mater. Sci. Eng. 626 (2015) 61–66, https://doi.org/10.1016/j.msea.2014.12.047.
[68] Y.F. Zhou, Z.Y. Zhao, X.Y. Tan, L.M. Luo, Y. Xu, X. Zan, Q. Xu, K. Tokunaga, X. Y. Zhu, Y.C. Wu, Densification and microstructure evolution of W-TiC-Y2O3 during spark plasma sintering, Int. J. Refract. Met. Hard Mater. 79 (2019) 95–101, https://doi.org/10.1016/j.ijrmhm.2018.11.014.
[69] V.R. Talekar, A. Patra, S.K. Sahoo, S.K. Karak, B. Mishra, Fabrication and characterization of nano-Y2O3, Al2O3, La2O3 dispersed mechanically alloyed and liquid phase sintered W-Ni for structural application, Int. J. Refract. Metals Hard Mater. 82 (2019) 183–198, https://doi.org/10.1016/j.ijrmhm.2019.03.027.
[70] B. Boztemur, Y.C. Gültekin, S. Ceylan, E. Görgün, O.H. Memiş, Y. Xu, L. Luo, M. L. Öveçoğlu, D. Ağaoğulları, MoB2/MoB ceramic particulate reinforced W-1 wt % Ni matrix composites as potential plasma facing materials, Ceram. Int. (2023), https://doi.org/10.1016/j.ceramint.2023.06.289.
[71] H. Gökçe, Ö. Balcı, D. Ağaoğulları, Ö.U. Demirkan, A. Genç, M.L. Öveçoğlu, Characterization investigations of WNi matrix composites reinforced with TiB2 and La2O3, 123 309–312, https://doi.org/10.12693/APhysPolA.123.309, 2013.
[72] D. Ağaoğulları, Ö. Balcı, O.U. Demirkan, H. Gökçe, A. Genç, M.L. Öveçoğlu, İ. Duman, Development of mechanically alloyed and sintered W-1 wt.% Ni matrix composites reinforced with TiB2, Solid State Phenom. 194 (2013) 194–198. https://doi.org/10.4028/www.scientific.net/SSP.194.194.
[73] Ö.U. Demirkan, A. Genç, M.L. Öveçoğlu, Effects of Al2O3 addition on the microstructure and properties of Ni activated sintered W matrix composites, J. Refract. Met. Hard Mater. 32 (2012) 33–38, https://doi.org/10.1016/j.ijrmhm.2012.01.004.
[74] Ö. Balcı, O.U. Demirkan, D. Ağaoğulları, H. Gökçe, A. Genç, M.L. Öveçoğlu, İ. Duman, Effects of La2O3 addition on the microstructure and properties of activated sintered W-Ni compacts, Solid State Phenom. 194 (2013) 217–221. https://doi.org/10.4028/www.scientific.net/SSP.194.217.
[75] S. Shivakumar, K. Song, C. Wang, T. Lei, H.L. Xin, T.J. Rupert, J. Luo, Discovery of Ni activated sintering of MoNbTaW predicted by a computed grain boundary diagram, Scripta Mater. 239 (2024) 115777, https://doi.org/10.1016/j.scriptamat.2023.115777.
[76] C. Suryanarayana, M.G. Norton, X-Ray Diffraction: A Practical Approach, 1998.
[77] Y. Xu, Y. Xu, Z. Wu, L. Luo, X. Zan, G. Yao, Y. Xi, Y. Wang, X. Ding, H. Bi, X. Zhu, Q. Xu, J. Wu, Y. Wu, Plasma-surface interaction experimental device: PSIEC and its first plasma exposure experiments on bulk tungsten and coatings, Fusion Eng. Des. 164 (2021) 1–7, https://doi.org/10.1016/j.fusengdes.2020.112198.
[78] S. Aydın, Metalurji ve malzeme mühendisleri için termodinamik. Literatür, 2015.
[79] A. Fu, Y. Cao, Y. Liu, S. Xu, Microstructure and mechanical properties of novel lightweight TaNbVTi-based refractory high entropy alloys, Materials 15 (2022) 355, https://doi.org/10.1016/j.commatsci.2023.112464.
[80] D. Ouyang, Z. jie Chen, H. bin Yu, K.C. Chan, L. Liu, Oxidation behavior of the Ti38V15Nb23Hf24 refractory high-entropy alloy at elevated temperatures, Corrosion Sci. 198 (2022) 110153, https://doi.org/10.1016/j.corsci.2022.110153.
[81] J. Liu, X. Zhao, S. Zhang, Y. Sheng, Q. Hu, Microstructure and mechanical properties of MoNbTaW refractory high-entropy alloy prepared by spark plasma sintering, J. Mater. Res. 38 (2023) 484–496, https://doi.org/10.1557/s43578-022-00833-6.
[82] T. Gu, L.M. Wang, Q. Hu, X. Bing, L. Dong, X. Fu, Y. Xiong, C. Xin, M. Zhao, Effect of mechanical alloying and sintering behavior on the microstructure and properties of NbMoTaWRe refractory high entropy alloy, Met. Mater. Int. 28 (2022) 2571–2582, https://doi.org/10.1007/s12540-021-01165-6.
[83] T. Xiang, M. Zhao, P. Du, G. Xie, Heat treatment effects on microstructure and mechanical properties of TiZrNbTa high-entropy alloy, J. Alloys Compd. 930 (2023) 167408, https://doi.org/10.1016/j.jallcom.2022.167408.
[84] T. Nagase, M. Todai, T. Hori, T. Nakano, Microstructure of equiatomic and non-equiatomic Ti-Nb-Ta-Zr-Mo high-entropy alloys for metallic biomaterials, J. Alloys Compd. 753 (2018) 412–421, https://doi.org/10.1016/j.jallcom.2018.04.082.
[85] S. Kanpara, S. Khirwadkar, S. Belsare, K. Bhope, R. Swamy, Y. Patil, Fabrication of tungsten & tungsten alloy and its high heat load testing for fusion applications, Mater. Today Proc. 3 (2016) 3055–3063, https://doi.org/10.1016/j.matpr.2016.09.020.
[86] J. Riesch, A. Feichtmayer, J.W. Coenen, B. Curzadd, H. Gietl, T. Höschen, A. Manhard, T. Schwarz-Selinger, R. Neu, Irradiation effects in tungsten—from surface effects to bulk mechanical properties, Nucl. Mater. Energy. 30 (2022) 101093, https://doi.org/10.1016/j.nme.2021.101093.
[87] C. Luo, L. Xu, L. Zong, H. Shen, S. Wei, Research status of tungsten-based plasma-facing materials: a review, Fusion Eng. Des. 190 (2023) 113487, https://doi.org/10.1016/j.fusengdes.2023.113487.
[88] H.W. Hayden, J.H. Brophy, The activated sintering of tungsten with group {VIII} elements, J. Electrochem. Soc. 110 (1963) 805, https://doi.org/10.1149/1.2425876.
[89] V.V. Panichkina, Activated sintering of tungsten with small additions of nickel, Sov, Powder Metall. Met. Ceram. 6 (1967) 87–90, https://doi.org/10.1007/BF00775635.
[90] M. Wang, Z.L. Ma, Z.Q. Xu, X.W. Cheng, Designing VxNbMoTa refractory high-entropy alloys with improved properties for high-temperature applications, Scripta Mater. 191 (2021) 131–136, https://doi.org/10.1016/j.scriptamat.2020.09.027.
[91] W.B. Pearson, The Crystal Chemistry and Physics of Metals and Alloys, Wiley-Inter-science, 1972.
[92] A. Genç, S. Coşkun, M.L. Öveçoğlu, Fabrication and properties of mechanically alloyed and Ni activated sintered W matrix composites reinforced with Y2O3 and TiB2 particles, Mater. Char. 61 (2010) 740–748, https://doi.org/10.1016/j.matchar.2010.04.006.
[93] S.R. Shatynski, The thermochemistry of transition metal carbides, Oxid. Metals 13 (1979) 105–118.
[94] C.C. Rudolf, Microstructure and Mechanical Properties of Nanofiller Reinforced Tantalum-Niobium Carbide Formed by Spark Plasma Sintering, Florida International University, 2016, https://doi.org/10.25148/etd.FIDC000728.
[95] J. Huang, Z. Cao, Z. Chen, Y. Li, Y. Ding, X. Liu, Effect of different pre-existing dislocation densities on the microstructure evolution of W-0.5ZrC alloy during in-situ He + irradiation, J. Nucl. Mater. 574 (2023) 154206, https://doi.org/10.1016/j.jnucmat.2022.154206.
[96] A. Lasa, S.K. Tähtinen, K. Nordlund, Loop punching and bubble rupture causing surface roughening —a model for W fuzz growth, Europhys. Lett. 105 (2014) 25002, https://doi.org/10.1209/0295-5075/105/25002.
[97] J. Wang, D. Liu, Z. Guo, B. He, W. Dang, Molecular dynamics study on the origin of fuzz structure on tungsten surface, J. Nucl. Mater. 547 (2021) 152835, https://doi.org/10.1016/j.jnucmat.2021.152835.
[98] J. Huang, Y. Li, G. Yuan, Q. Liu, T. Zuo, G. Xu, J. Lv, X. Ding, Y. Hong, L. Luo, X. Tan, J.L. Chen, Y. Wu, Corrosion and microstructure evolution of He+ plasma irradiated tungsten PFMs, Fusion Eng. Des. 184 (2022) 113279, https://doi.org/10.1016/j.fusengdes.2022.113279.
[99] G. Pu, K. Zhang, L. Yang, Y. Luo, S. Chen, J. Li, Y. Xue, B. Liu, H. Yang, Z. Ye, F. Gou, C. Yang, Z. Wang, Y. Wang, Irradiation-enhanced superficial modification and evolution of mechanical behavior in TaTiNbZr refractory high entropy alloy films exposed to low energy helium plasma, 577, https://doi.org/10.1016/j.jnucmat.2023.154337, 2023.
[100] J. Wang, L. Yang, S. Yang, Y. Jia, M. Chen, Y. Qiao, P. Guo, S. Zhu, F. Wang, Effect of γ phase elements on oxidation behavior of nanocrystalline coatings at 1050 0C, Materials 14 (2021) 202, https://doi.org/10.3390/ma14010202.
[101] T. Cheng, G. Wei, S. Jiang, J. Zhang, Y. Wang, P. Liu, M. Hong, E. Guo, F. Zhong, G. Cai, C. Jiang, F. Ren, Enhanced resistance to helium irradiations through unusual interaction between high-entropy-alloy and helium, Acta Mater. 248 (2023) 118765, https://doi.org/10.1016/j.actamat.2023.118765.
[102] H. Zhang, C. Li, Z. Zhu, H. Huang, Y. Lu, T. Wang, Effects of He-ion irradiation on the microstructures and mechanical properties of the novel Co-free Vx CrFeMnNiy high-entropy alloys, J. Nucl. Mater. 572 (2022) 154074, https://doi.org/10.1016/j.jnucmat.2022.154074.
[103] G. Ackland, Controlling radiation damage, Science 327 (2010) 1587–1588.
[104] O. El-Atwani, J.A. Hinks, G. Greaves, J.P. Allain, S.A. Maloy, Grain size threshold for enhanced irradiation resistance in nanocrystalline and ultrafine tungsten, Mater. Res. Lett. 5 (2017) 343–349, https://doi.org/10.1080/21663831.2017.1292326.
[105] H.C. Kim, E. Bang, N. Kwak, Y. Oh, H.N. Han, H. Choi, K. Kim, S.H. Hong, Thermal and microstructural properties of spark plasma sintered tungsten for the application to plasma facing materials, Fusion Eng. Des. 146 (2019) 2649–2653, https://doi.org/10.1016/j.fusengdes.2019.04.071.
[106] O. El Atwani, H.T. Vo, M.A. Tunes, C. Lee, A. Alvarado, A quinary WTaCrVHf nanocrystalline refractory high-entropy alloy withholding extreme irradiation environments, Nat. Commun. 14 (2023) 2516, https://doi.org/10.1038/s41467-023-38000-y.
[107] M. Moschetti, A. Xu, B. Schuh, A. Hohenwarter, J. Couzinie, On the room-temperature mechanical properties of an ion-irradiated TiZrNbHfTa refractory high entropy alloy, 72, https://doi.org/10.1007/s11837-019-03861-6, 2020.
[108] O. Waseem, H. Ryu, Helium ions irradiation analysis of W 0.5(TaTiVCr)0.5 for application as a future fusion plasma-facing material, Mater. Chem. Phys. 260 (2021) 124198, https://doi.org/10.1016/j.matchemphys.2020.124198.
[109] L. Zhang, Y. Du, W. Han, X. Yi, P. Liu, K. Yoshida, T. Toyama, C. Xu, Q. Zhan, Y. Nagai, S. Ohnuki, F. Wan, The neglected activation of tantalum in reduced activation materials, Nucl. Mater. Energy. 35 (2023) 101432, https://doi.org/10.1016/j.nme.2023.101432.